TOR VERGATA
UNIVERSITÀ DEGLI STUDI DI ROMA

Galaxy cluster atmospheres as jointly seen by the South Pole Telescope, Chandra and Planck satellites

Claudio Mastromarino

claudio.mastromarino@roma2.infn.it
Università degli studi di Roma Tor Vergata
H. Bourdin, P. Mazzotta, F. De Luca, F. Oppizzi

mm-Universe 2025
23/06/2025

Overview

- **How can we get ICM properties (Thermodynamic profiles/Hydrostatic mass) in regions where X-ray spetroscopy fails?**
- **Can a joint (X-ray/mm) analysis give new inputs on the cross-calibration issues?**

C. Mastromarino, F. Oppizzi, F. De Luca, H. Bourdin, P. Mazzota, (2024), "**Resolving high-z Galaxy Cluster properties through joint X-ray and Millimeter analysis: a case study of SPT-CLJ0615-5746**."A&A, 688, A76. https://doi.org/10.1051/0004-6361/202449422

- Methods
- Results of SPT0615

C. Mastromarino, F. De Luca, H. Bourdin, P. Mazzota, F. Oppizzi "**Hydrostatic Mass and Baryon Fraction of Galaxy Clusters: A Joint X-ray and Millimeter Analysis of 23 SPT-SZ Selected Clusters**", (Under int. review)

- Hydrostatic Mass / Hydrostatic gas fraction
- Comparison with catalogs

Multiwavelenght observations

The majority of baryons in cluster are in the form of a high ionized atmosphere (ICM) detectable at the same time in both **X-ray** and **millimeter** bands.

- **Thermal Bremsstrahlung** of the hot ($T \sim 10^8 K$) ICM

$$\Sigma_X(r_{2D}) = \frac{1}{4\pi(1+z)^3} \int \frac{n_e^2(r_{3D})}{x} \Lambda(T, Z)\, dl$$

- Inverse Compton scattering of CMB **(Sunyaev-Zel'dovich effect)**

$$y_{SZ}(r_{2D}) = \frac{\sigma_T}{m_e c^2} \int P_e(r_{3D}) dl$$

$$= \frac{\sigma_T}{m_e c^2} \int n_e(r_{3D}) k_B T_e(r_{3D}) dl$$

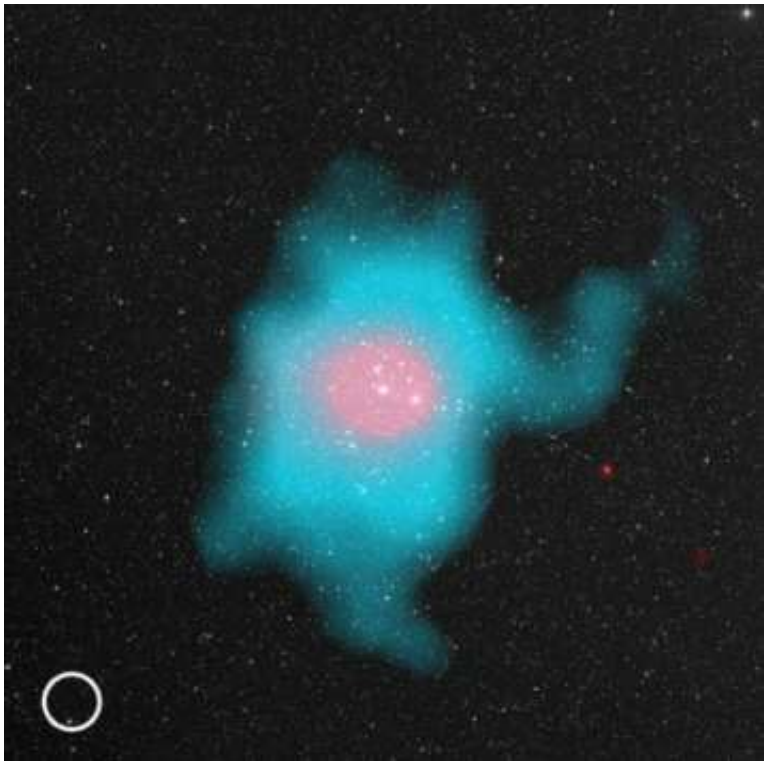

Composite images of the optical (DSS, white), X-ray (ROSAT, pink) and SZ signal (Planck, blue), of the Perseus cluster.

Multiwavelenght observations

The majority of baryons in cluster are in the form of a high ionized atmosphere (ICM) detectable at the same time in both **X-ray** and **millimeter** bands.

- **Thermal Bremsstrahlung** of the hot ($T \sim 10^8 K$) ICM

$$\Sigma_X(r_{2D}) = \frac{1}{4\pi(1+z)^3} \int \frac{n_e^2(r_{3D})}{x} \Lambda(T,Z)\, dl$$

- Inverse Compton scattering of CMB (**Sunyaev-Zel'dovich effect**)

$$y_{SZ}(r_{2D}) = \frac{\sigma_T}{m_e c^2} \int P_e(r_{3D}) dl$$

$$= \frac{\sigma_T}{m_e c^2} \int n_e(r_{3D}) k_B T_e(r_{3D}) dl$$

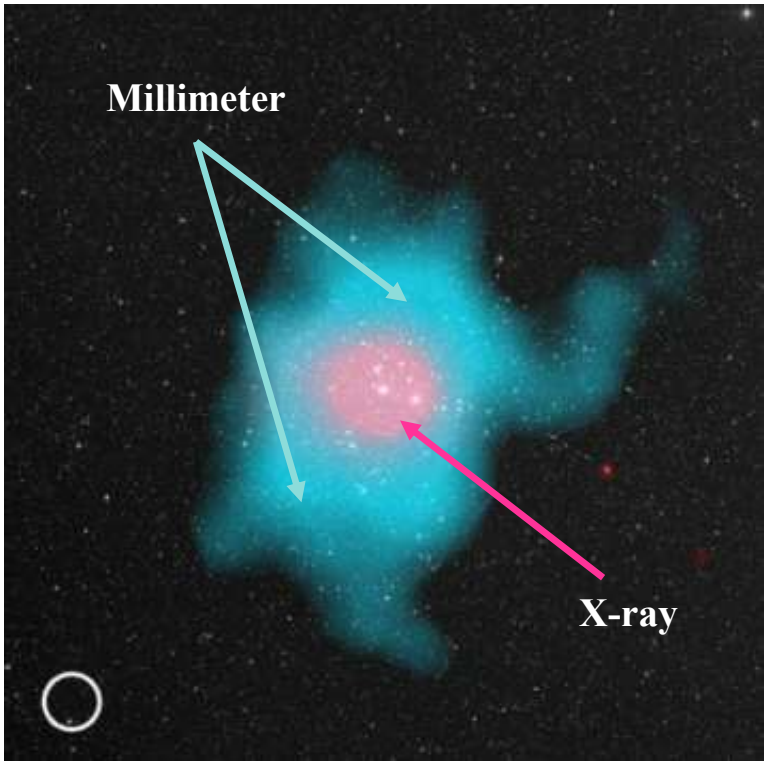

Composite images of the optical (DSS, white), X-ray (ROSAT, pink) and SZ signal (Planck, blue), of the Perseus cluster.

Multiwavelenght observations

The majority of baryons in cluster are in the form of a high ionized atmosphere (ICM) detectable at the same time in both **X-ray** and **millimeter** bands.

- **Thermal Bremsstrahlung** of the hot ($T \sim 10^8 K$) ICM

$$\Sigma_X(r_{2D}) = \frac{1}{4\pi(1+z)^3} \int \frac{n_e^2(r_{3D})}{x} \Lambda(T,Z)\, dl$$

- Inverse Compton scattering of CMB (**Sunyaev-Zel'dovich effect**)

$$y_{SZ}(r_{2D}) = \frac{\sigma_T}{m_e c^2} \int P_e(r_{3D}) dl$$

$$= \frac{\sigma_T}{m_e c^2} \int n_e(r_{3D}) k_B T_e(r_{3D}) dl$$

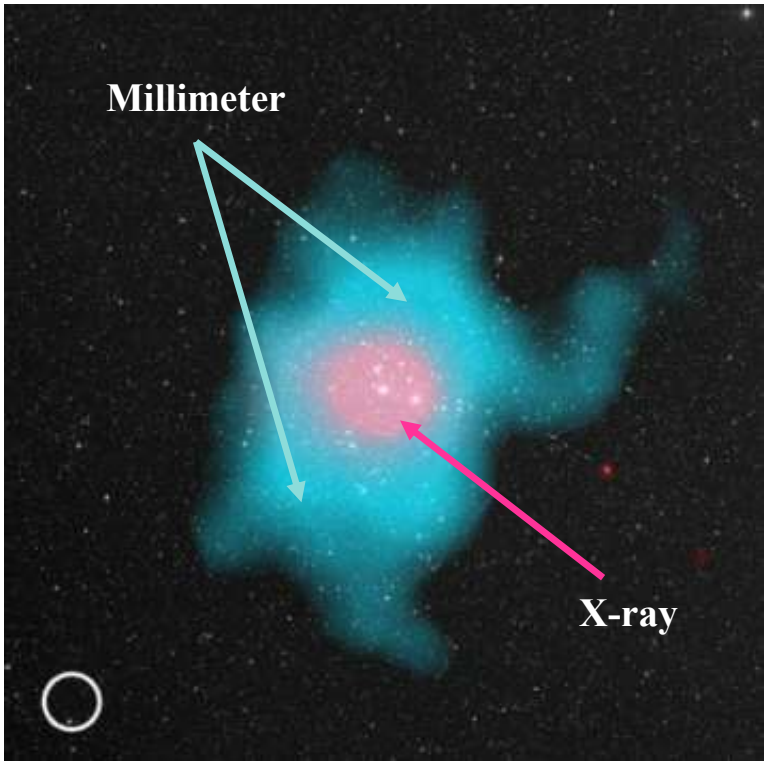

Composite images of the optical (DSS, white), X-ray (ROSAT, pink) and SZ signal (Planck, blue), of the Perseus cluster.

The η_T parameter

We must consider the possibility of systematics in this combination (**cross-calibration** between instruments**,** **morphologial properties**, **cosmological model**). These factors can introduce discrepancies between the two independent observations of the gas.
Such systematics can be accounted for by introducing the normalization parameter η_T.
It represents the normalization between X-ray and SZ inferences of the ICM

$$P_X = \eta_T \times P_{SZ} \rightarrow kT_X = \eta_T \times P_{SZ}/n_e$$

Since we observe the same gas, in the ideal scenario $\boldsymbol{\eta_T = 1}$. In more realistic scenario, η_T is expected to deviate from one.

$$\eta_T = \mathcal{C} \times \mathcal{B} \times b_n$$

The η_T parameter

We must consider the possibility of systematics in this combination (**cross-calibration** between instruments**,** **morphologial properties**, **cosmological model**). These factors can introduce discrepancies between the two independent observations of the gas.
Such systematics can be accounted for by introducing the normalization parameter η_T.
It represents the normalization between X-ray and SZ inferences of the ICM

$$P_X = \eta_T \times P_{SZ} \rightarrow kT_X = \eta_T \times P_{SZ}/n_e$$

Since we observe the same gas, in the ideal scenario $\boldsymbol{\eta_T = 1}$. In more realistic scenario, η_T is expected to deviate from one.

$$\eta_T = \mathcal{C} \times \mathcal{B} \times b_n$$

- **Cosmology:** Different dependencies on the **cosmic distance** and **chemical composition** of the gas

$$n_e \propto D(z)_A^{-3/2} \qquad P_{SZ} \propto D(z)_A^{-1} \qquad \Sigma_X \propto \Lambda(T, H, Y) = \Lambda_H \times (1 + 4n_{He}/n_p)$$

$$\mathcal{C} \propto D(z)_A^{-1/2} \times Y^{-1/2}$$

The η_T parameter

We must consider the possibility of systematics in this combination (**cross-calibration** between instruments**,** **morphologial properties**, **cosmological model**). These factors can introduce discrepancies between the two independent observations of the gas.
Such systematics can be accounted for by introducing the normalization parameter η_T.
It represents the normalization between X-ray and SZ inferences of the ICM

$$P_X = \eta_T \times P_{SZ} \rightarrow kT_X = \eta_T \times P_{SZ}/n_e$$

Since we observe the same gas, in the ideal scenario $\boldsymbol{\eta_T = 1}$. In more realistic scenario, η_T is expected to deviate from one.

$$\eta_T = \mathcal{C} \times \mathcal{B} \times b_n$$

- **Cosmology:** Different dependencies on the **cosmic distance** and **chemical composition** of the gas

$$n_e \propto D(z)_A^{-3/2} \qquad P_{SZ} \propto D(z)_A^{-1} \qquad \Sigma_X \propto \Lambda(T, H, Y) = \Lambda_H \times (1 + 4n_{He}/n_p)$$

$$\mathcal{C} \propto D(z)_A^{-1/2} \times Y^{-1/2}$$

- **Geometry:** Departure from the spherical symmetry (**asphericity**) and **clumpiness** of the gas

$$\mathcal{B} \propto C_\rho^{1/2}/e_{LOS}^{1/2}$$

- $\boldsymbol{b_n}$ **:** Other potential systematics due to uncertainties in **the calibration of X-ray spectroscopic temperature** or assumptions and approximations in our methodology, such as profile modeling or the fitting procedure

SPT-CLJ0615-5746

The highest-redshift cluster ($z = 0.972$) detected by **Planck** (S/N=7.8) and it also belongs to the **SPT**-SZ catalog (S/N=26.4).
With $M_{500}^{SPT} = 10.16^{+0.98}_{-1.20}\ 10^{14}\ M_{\odot}$ is one of the most massive cluster in the survey.
It has additionally been observed with **Chandra** ($t_{exp} \sim 240ks$).

The X-ray and the SZ analyses are based on an updated version of Bourdin et al. (2017) and Oppizzi et al. (2023).

X-ray denoising:

- Point sources mask;
- **Parametric modeling** of the foreground/background contribution (Particle background, CXB, Galaxy foreground);
- Identification of the X-ray peak.

SZ denoising:

- Point sources mask;
- Planck multicomponent separation (GTD and CMB);
- SPT Internal Linear Combination (CMB).
- Both **local denoising** of the contaminants.

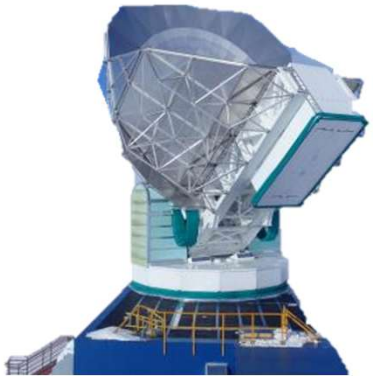

X-ray observables

Using the X-ray peak, we extracted the radial profiles of the background-subtracted X-ray observable: the **surface brightness (Σ_X)** and the **spectroscopic temperature (T_{spec}).**

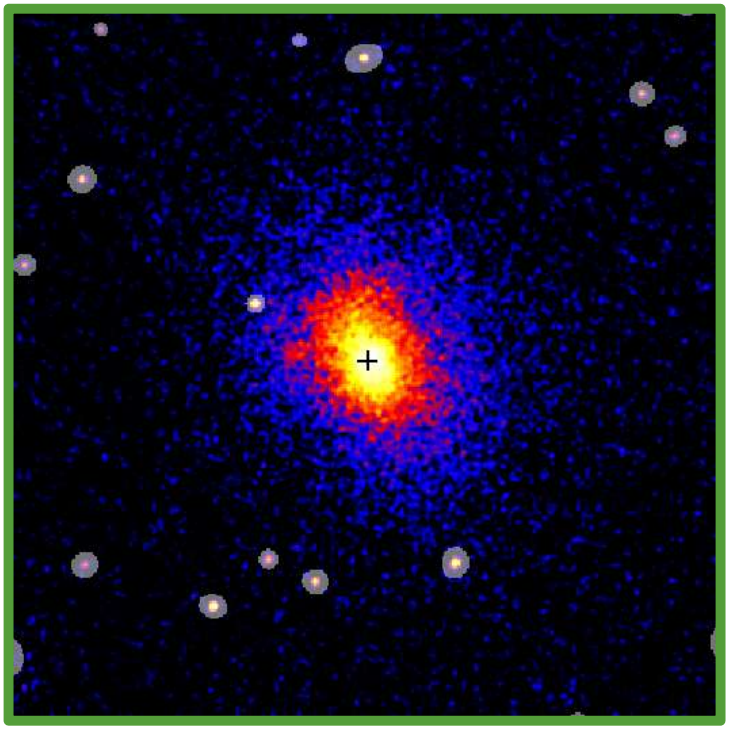

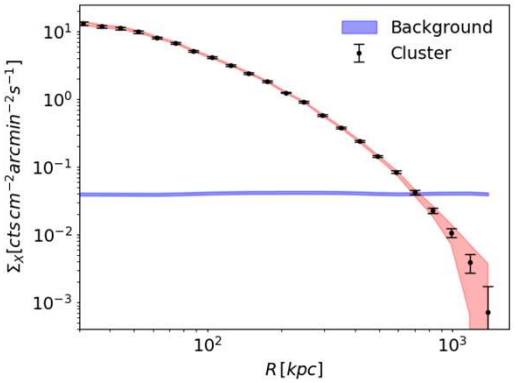

$R > 1.2\ R_{500}^{SPT}$:
$\sim 10\ times\ below\ the\ bck$

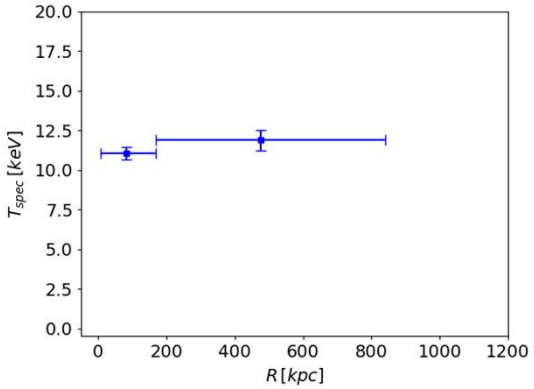

$R > 0.8\ R_{500}^{SPT}$:
$S/N \sim 10\%$

X-ray observables

Using the X-ray peak, we extracted the radial profiles of the background-subtracted X-ray observable: the **surface brightness (Σ_X)** and the **spectroscopic temperature (T_{spec}).**

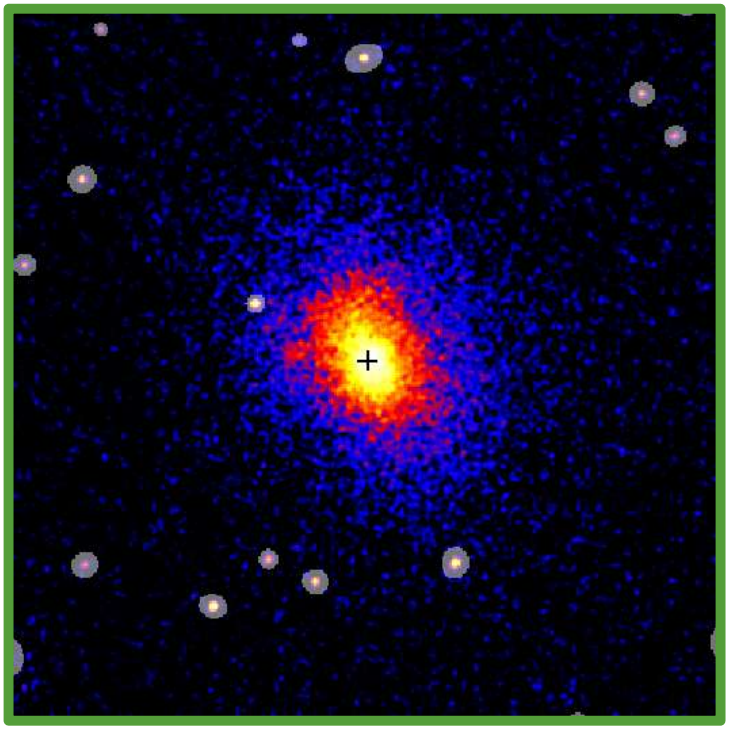

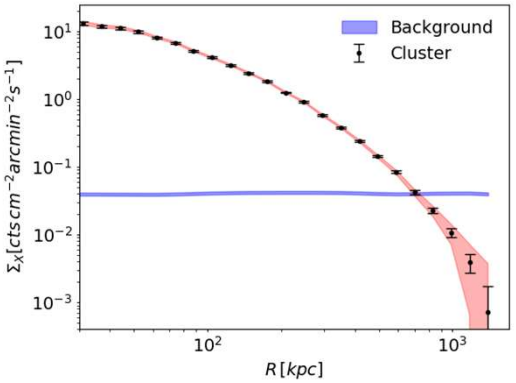

$R > 1.2\ R_{500}^{SPT}$:
$\sim 10\ times\ below\ the\ bck$

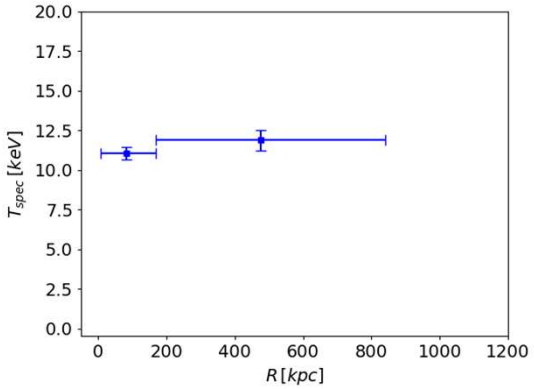

Need Joint Fit

$R > 0.8\ R_{500}^{SPT}$:
$S/N \sim 10\%$

Millimeter observables

For each cleaned map we calculated the **radial SZ profiles** centered on the X-ray peak.
We use d the **95 and 150** GHz channels of SPT and the **100, 143, and 353** GHz channels of Planck.
We expect low S/N at higher frequencies.

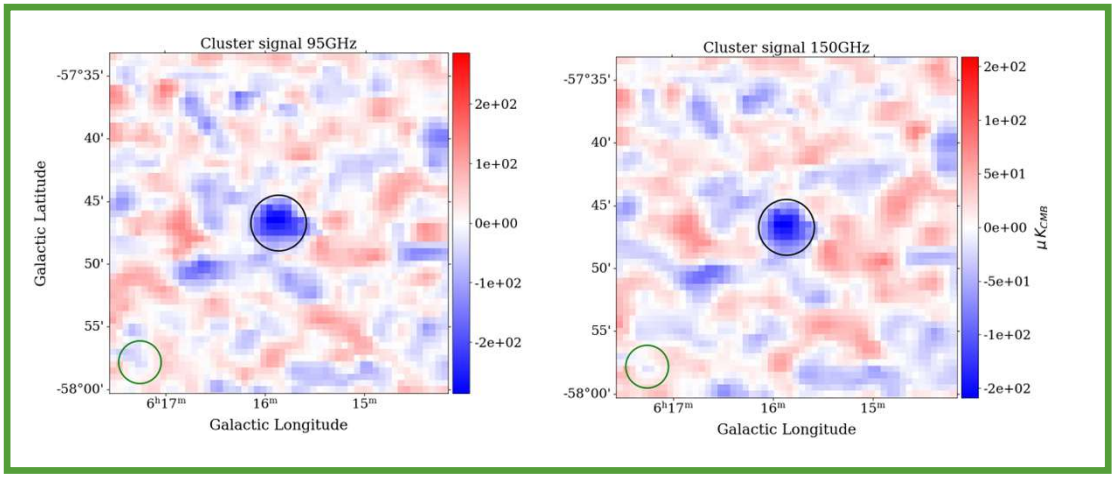

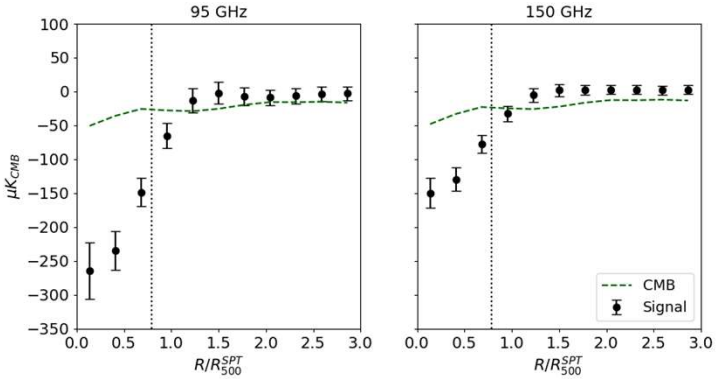

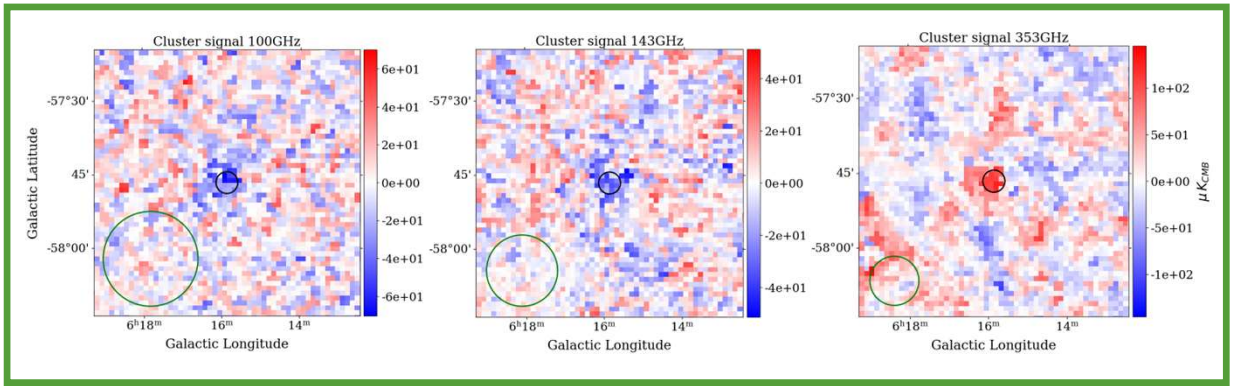

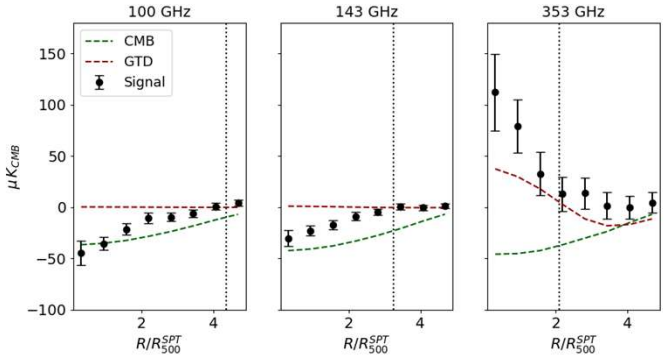

X-ray density profile

We parameterize the emission measure profile using analytical forms first proposed in Vikhlinin et al. (2006) and integrated it along the line of sight and fitted to the surface brightness profile Σ_X.

$\boldsymbol{n_e(r)}$

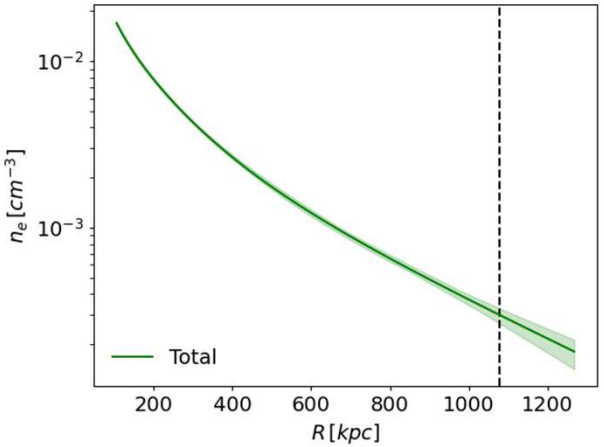

X-ray density profile

We parameterize the emission measure profile using analytical forms first proposed in Vikhlinin et al. (2006) and integrated it along the line of sight and fitted to the surface brightness profile Σ_X.

$$\boldsymbol{n_e(r)}$$

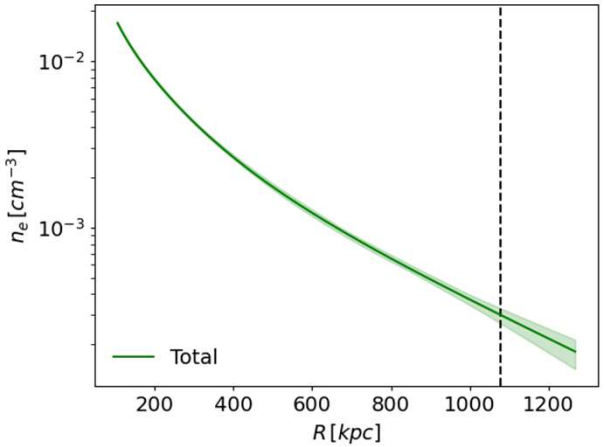

Joint Pressure profile

We assume that the pressure structure follows the spherically symmetric profile proposed by Nagai et. al (2007). We use this model to build:

- **Thermal SZ template**

$$I_{SZ,c} = s_{SZ,c}\,\frac{\sigma_T}{m_e c^2}\int P(r)dl$$

- **Temperature template**

$$kT(r) = \eta_T \times \frac{P(r)}{n_e}$$

We **joint fitted** the two template on the SZ brightness profiles and spectroscopic temperature, respectively.

$$P_{SZ,X} = \eta_T \times P(r)$$

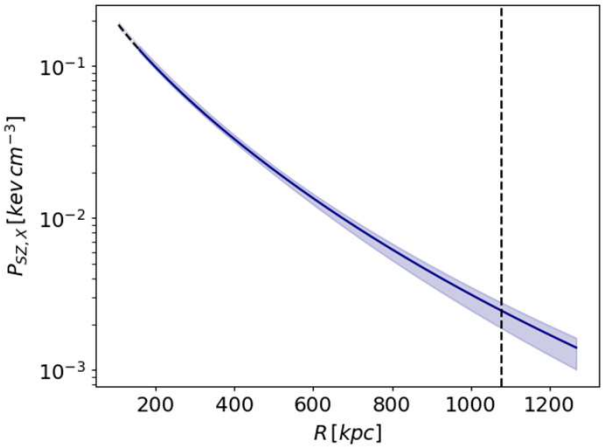

X-ray density profile

We parameterize the emission measure profile using analytical forms first proposed in Vikhlinin et al. (2006) and integrated it along the line of sight and fitted to the surface brightness profile Σ_X.

$$\boldsymbol{n_e(r)}$$

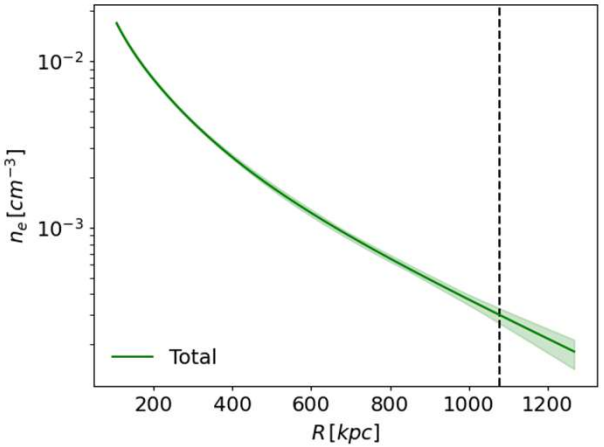

Joint Pressure profile

We assume that the pressure structure follows the spherically symmetric profile proposed by Nagai et. al (2007). We use this model to build:

- **Thermal SZ template**

$$I_{SZ,c} = s_{SZ,c}\,\frac{\sigma_T}{m_e c^2}\int P(r)dl$$

- **Temperature template**

$$kT(r) = \eta_T \times \frac{P(r)}{n_e}$$

We **joint fitted** the two template on the SZ brightness profiles and spectroscopic temperature, respectively.

$$P_{SZ,X} = \eta_T \times P(r)$$

$$\eta_T = 1.45 \pm 0.17$$

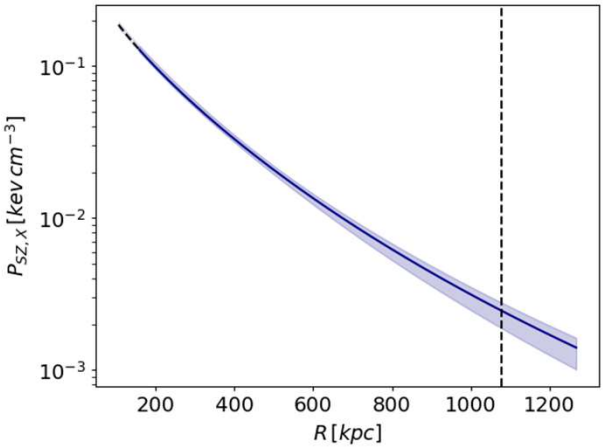

Thermodynamic profiles and Hydrostatic mass

At the end of our fitting procedure, we are left with the density profile from Chandra observations (n_e) and the Pressure profile from our joint analysis ($P_{SZ,X} = \eta_T \times P$).

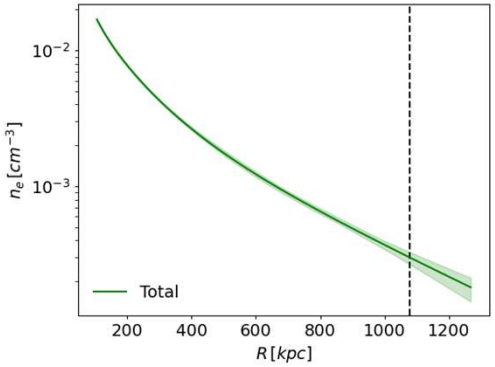

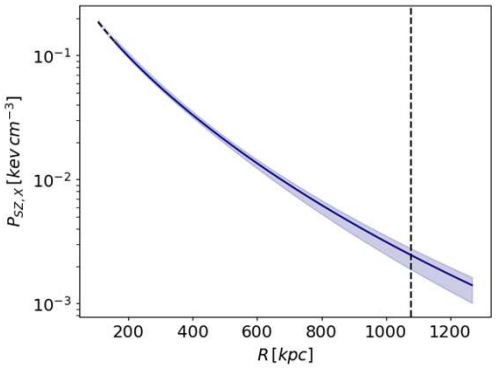

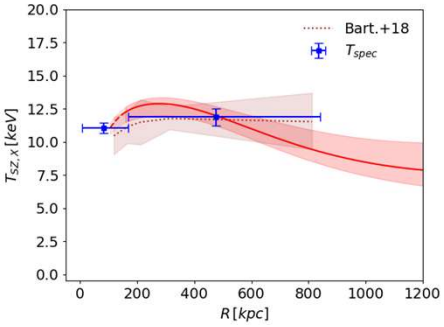

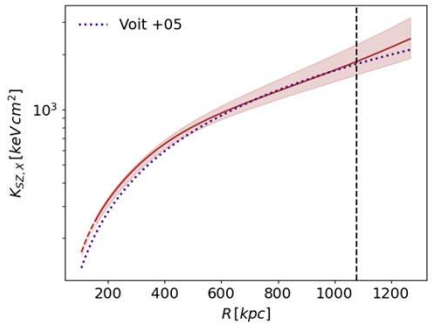

$$kT_{SZ,X}(r) = \eta_T \frac{P(r)}{n_e(r)}$$

$$K_{SZ,X}(r) = \eta_T \frac{P(r)}{n_e^{5/3}(r)}$$

Thermodynamic profiles and Hydrostatic mass

At the end of our fitting procedure, we are left with the density profile from Chandra observations (n_e) and the Pressure profile from our joint analysis ($P_{SZ,X} = \eta_T \times P$).

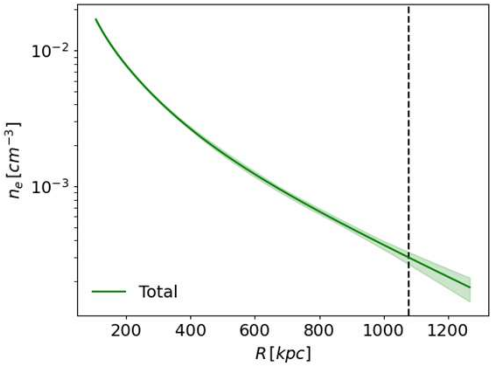

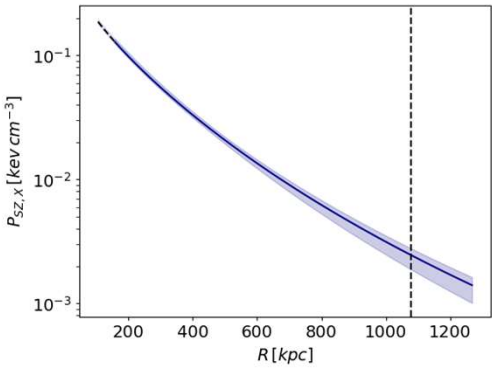

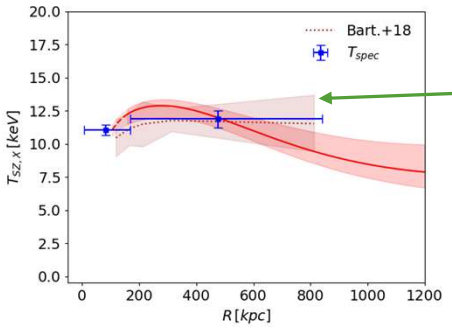

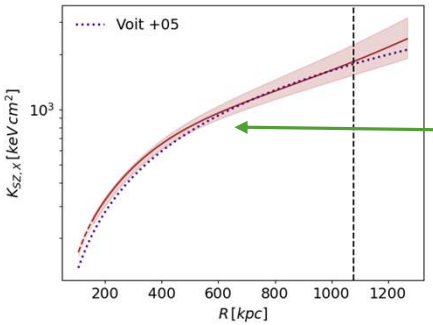

Good agreement with the 3D temperature derived from an X-ray only.

Good agreement with the simulated entropy profile.

Thermodynamic profiles and Hydrostatic mass

At the end of our fitting procedure, we are left with the density profile from Chandra observations (n_e) and the Pressure profile from our joint analysis ($P_{SZ,X} = \eta_T \times P$).

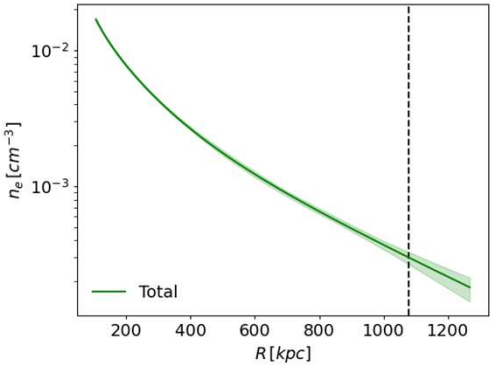

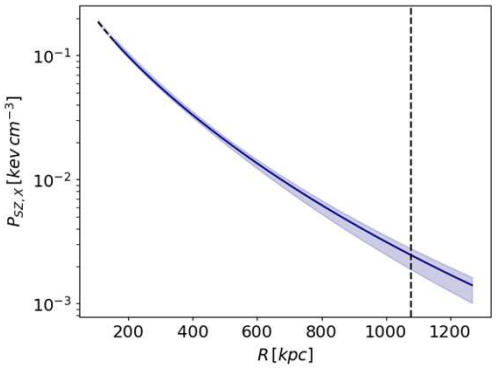

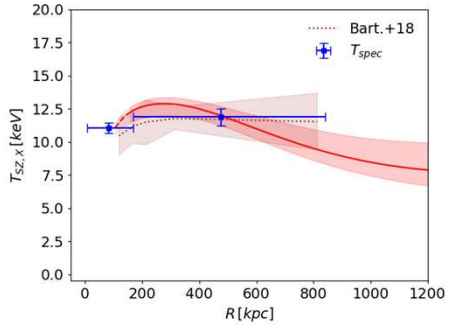

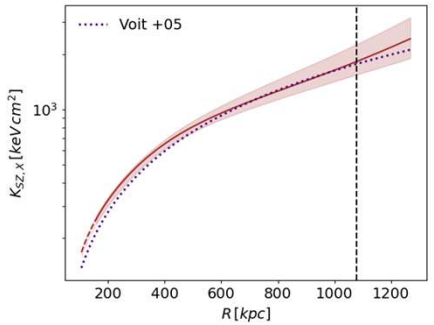

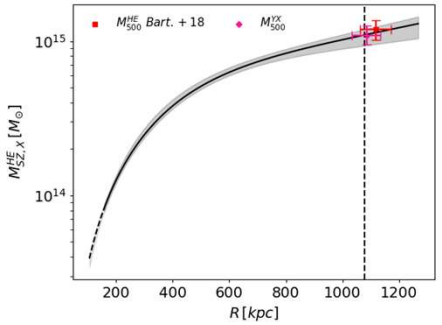

$$kT_{SZ,X}(r) = \eta_T \frac{P(r)}{n_e(r)}$$

$$K_{SZ,X}(r) = \eta_T \frac{P(r)}{n_e^{5/3}(r)}$$

$$M^{HE}_{SZ,X}(< R) = -\eta_T \frac{r^2}{G\,\mu\,m_p n_e(r)} \frac{dP(r)}{dr}$$

Thermodynamic profiles and Hydrostatic mass

At the end of our fitting procedure, we are left with the density profile from Chandra observations (n_e) and the Pressure profile from our joint analysis ($P_{SZ,X} = \eta_T \times P$).

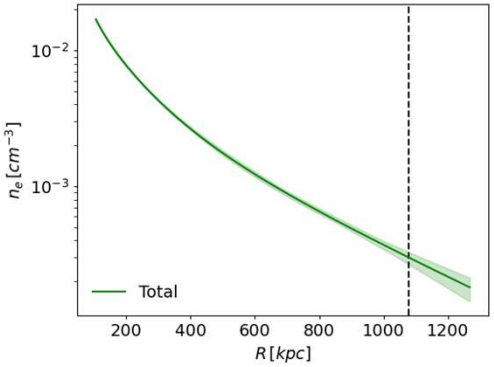

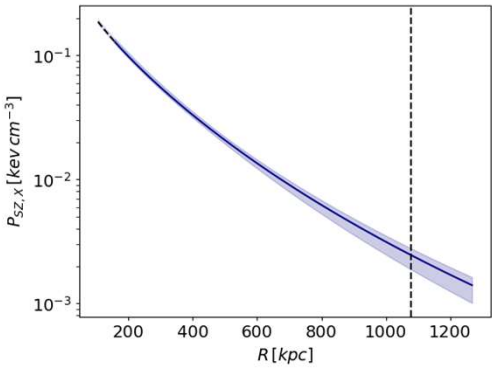

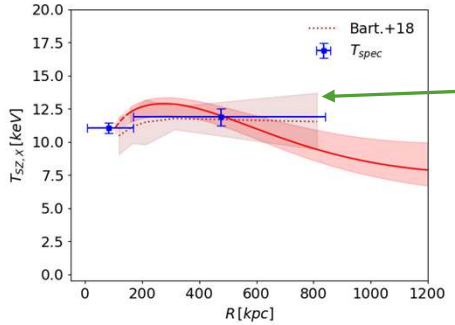

Good agreement with the 3D temperature derived from an X-ray only.

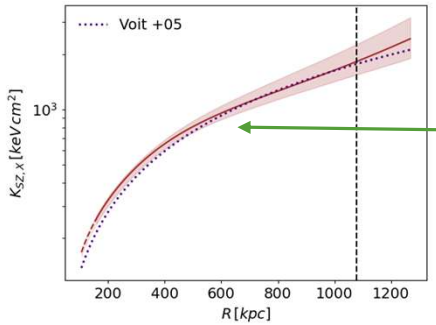

Good agreement with the simulated entropy profile.

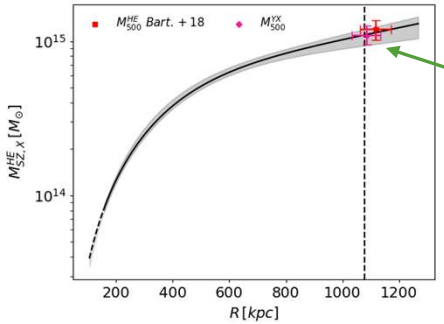

Good agreement with both the SPT estimation and with previous results from an X-ray only estimates

Summary

- As detailed in Mastromarino et al. (2024), the multiwavelenght approach allows us to constrain the thermodynamic profiles across **a wider range of spacial scales** compared to a SZ-only or X-ray-only analysis.

- The high angular resolution provided by Chandra facilitates a more precise constraint on the shape of the pressure profile within the inner region of the cluster, compared to an SZ-only analysis.

- The SZ observations allows us to extend our coverage to **a radial range primarily limited by our ability to extract a density profile rather than by the availability of spectroscopic temperature measurements.**
  This highlights the potential of our method to provide insights into thermodynamic profiles and hydrostatic mass of galaxy clusters at large radii, even in cases where obtaining accurate spectroscopic temperature data is challenging.

- Our analysis reveals a **high value for the normalization parameter** ($\eta_T = 1.45$). We observe a significant deviation from the ideal case ($\eta_T = 1$). This suggests that a straightforward combination of Chandra X-ray and millimetric data, without accounting for systematic differences, is not feasible. This highlights the importance of incorporating a normalization parameter in our analysis, as it encodes these systematic.

- Both our hydrostatic mass and temperature profiles are **consistent in the radial range covered from previous analysis** of this system. This consistency provides confidence in extending trust to our results at larger scales.

Sample

$0.16 < z < 0.61$

$5.08 < M_{500}^{SPT}/10^{14}\, M_{\odot} < 15.71$

- 23 galaxy clusters selected based on their SZ properties from the 2500-square-degree SPT-SZ catalog (Bleem et al. 2015), with an SZ significance of S/R>7.0.
- All clusters have also been detected by Planck via SZ effects (Planck Collaboration et al. 2016).
- Reliable Chandra observations to extract at least **two spectroscopic temperature** bins **up to 0.8** R_{500}.

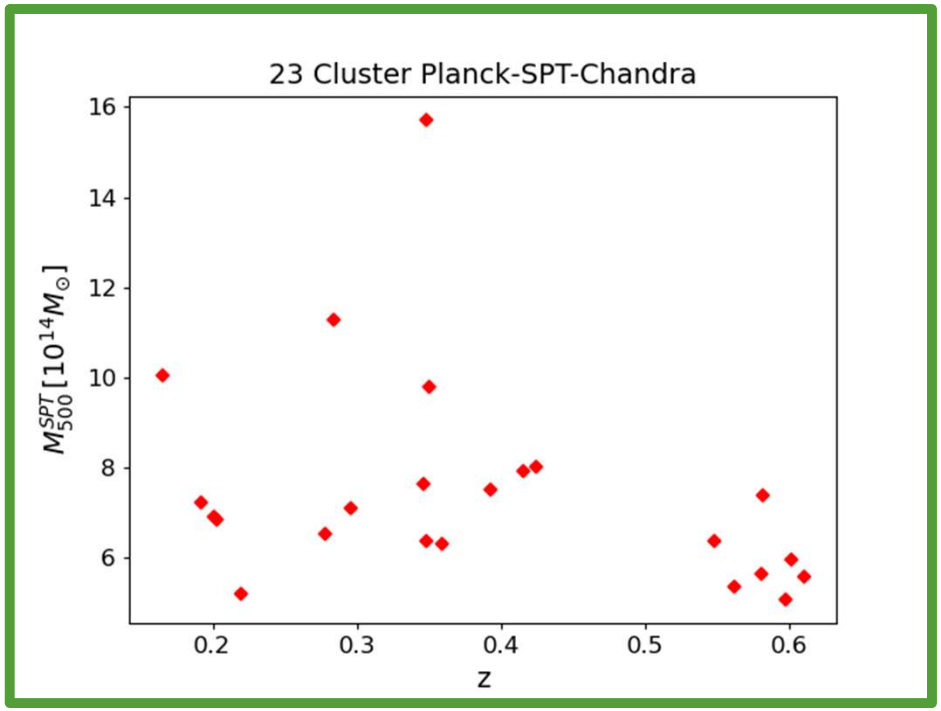

Pipeline

1. Modeling and subtraction of the X-ray and millimeter backgrounds (cleaned Maps);
2. Radial profile of the X and SZ observables;
3. X-ray density profile fitting;
4. Joint X/SZ pressure profile fitting.

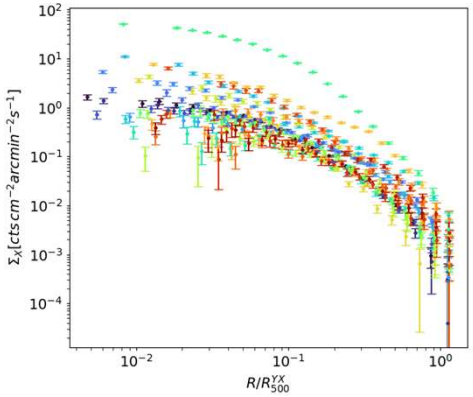

$n_e(r)$

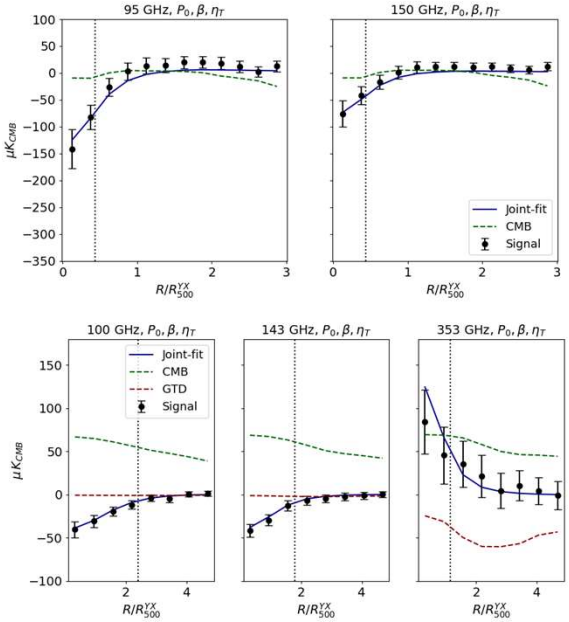

$$I_{SZ,c} = s_{SZ,c}\,\frac{\sigma_T}{m_e c^2}\int P(r)dl$$

$$kT(r) = \eta_T \times \frac{P(r)}{n_e}$$

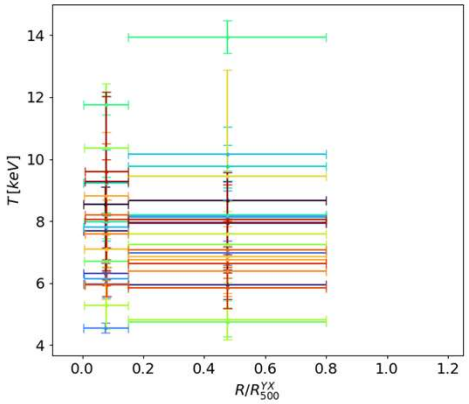

η_T distribution

The joint X-ray and SZ extraction of the cluster pressure profiles provides a normalization between the two signals, through the η_T parameter.

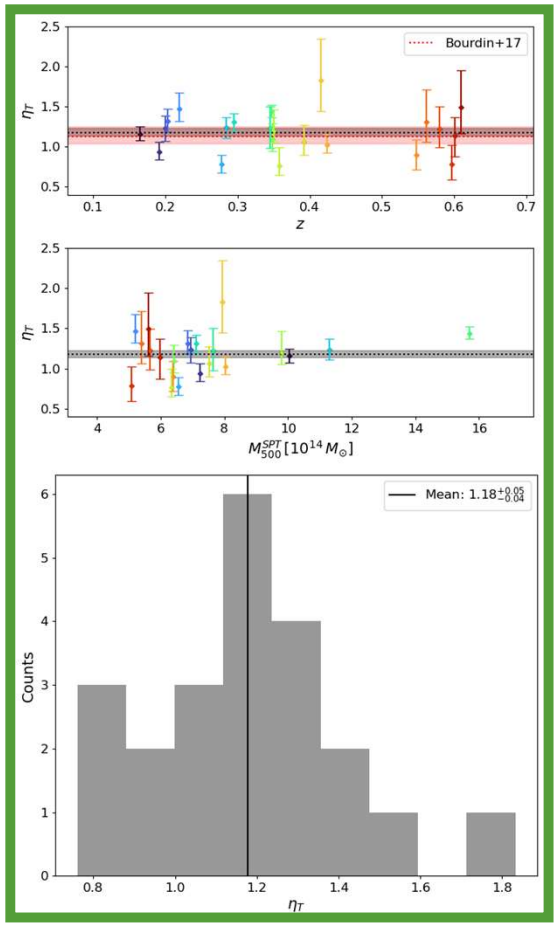

- Agreement (5% higher) respect to previous estimates from joint **Chandra**-Planck analysis:

  -Bourdin et al. (2017): $\eta_T = 1.13^{+0.10}_{-0.09}$

  -Wan et al. (2021): $\eta_T = 1.13^{+0.09}_{-0.09}$

- On average, our mean value is around 20% higher than the mean values from X-ray/SZ joint fit based on **XMM-Newton** data.

η_T distribution

The joint X-ray and SZ extraction of the cluster pressure profiles provides a normalization between the two signals, through the η_T parameter.

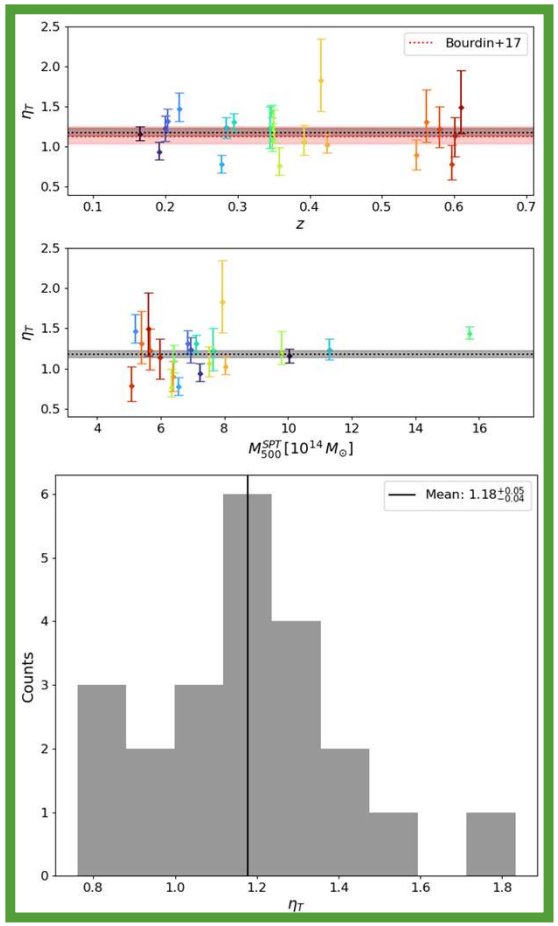

- Agreement (5% higher) respect to previous estimates from joint **Chandra**-Planck analysis:

-Bourdin et al. (2017): $\eta_T = 1.13^{+0.10}_{-0.09}$

-Wan et al. (2021): $\eta_T = 1.13^{+0.09}_{-0.09}$

- On average, our mean value is around 20% higher than the mean values from X-ray/SZ joint fit based on **XMM-Newton** data.

↓

Cross-calibration between intstruments

Cluster temperatures are known to be discrepant between Chandra and XMM, with Chandra temperature being on average 15% higher than XMM temperature.

It increases the η_T parameter of the same amount

Hydrostatic Masses

$$M_X^{HE}(< R) = -\eta_T \frac{r^2}{G\,\mu\,m_p n_e(r)} \frac{dP\,(r)}{dr}$$

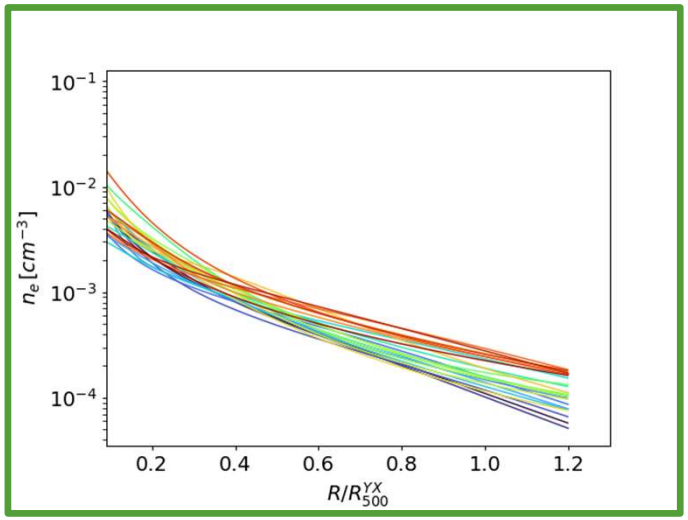

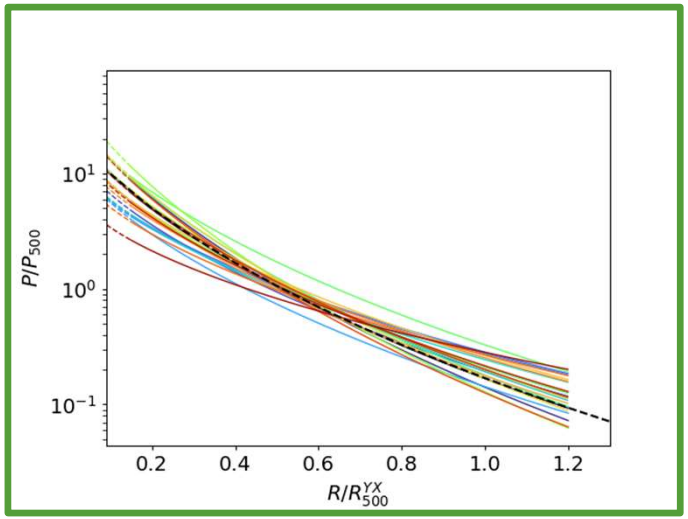

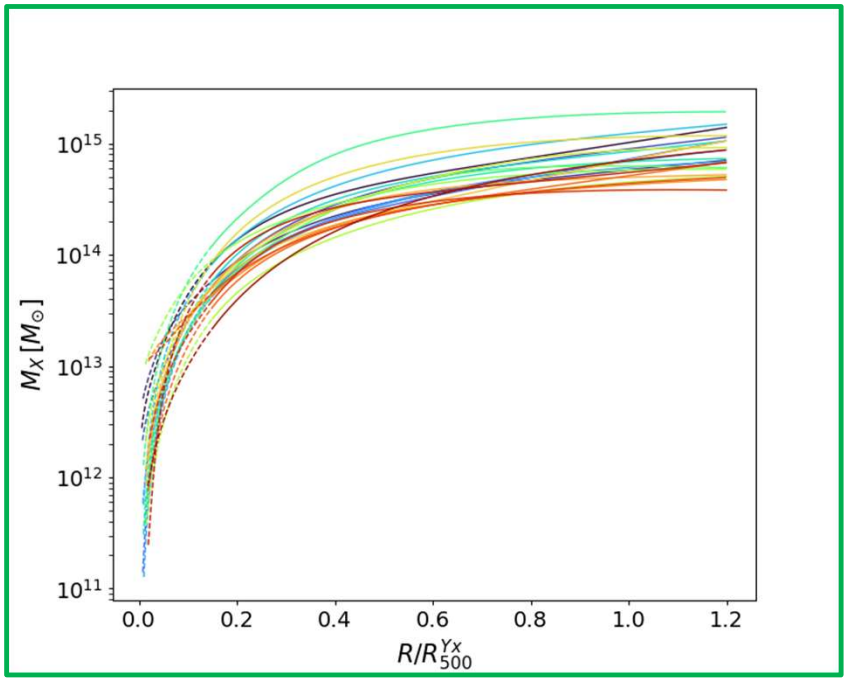

Hydrostatic mass comparison

We compare the hydrostatic mass estimates obtained from our joint fit with other mass estimates derived from other catalogs. To make a meaningful comparison, we interpolate our mass profiles at the radii corresponding to the locations of the other mass estimates.

eRosita

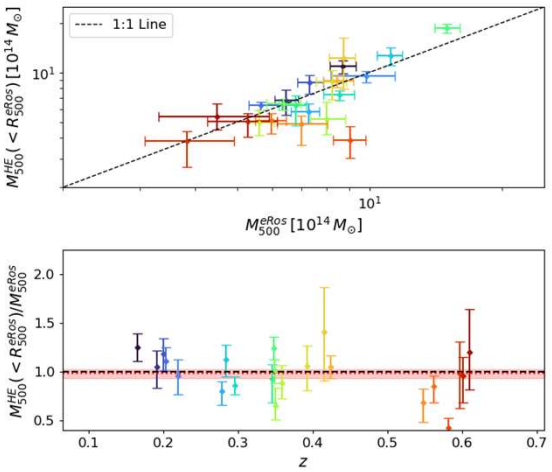

$$< \frac{M_{X,500}^{HE}}{M_{500}^{eRos}} > = 0.98 \pm 0.04$$

SPT

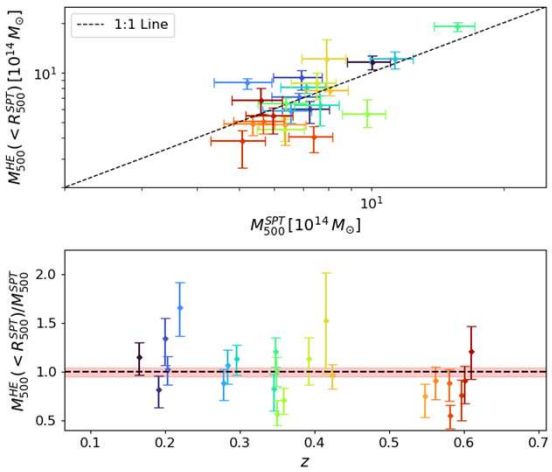

$$< \frac{M_{X,500}^{HE}}{M_{500}^{SPT}} > = 0.99 \pm 0.04$$

Planck

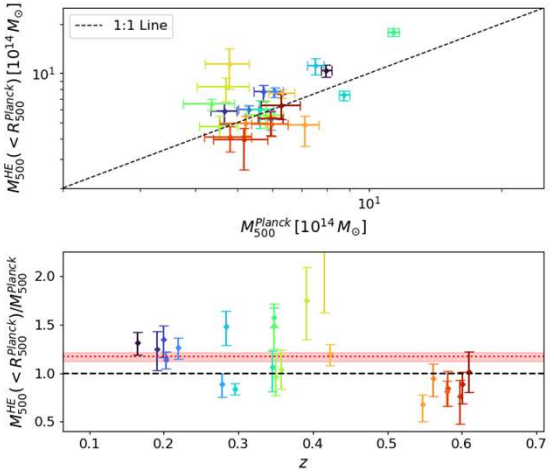

$$< \frac{M_{X,500}^{HE}}{M_{500}^{Planck}} > = 1.15 \pm 0.04$$

- Our hydrostatic mass are consistent with the mass estimates from SPT and eRosita catalogs (**WL calibrated masses**).
- Our masses are around 15% higher than the mass esitmates from Planck catalog.

Hydrostatic mass comparison

We compare the hydrostatic mass estimates obtained from our joint fit with other mass estimates derived from other catalogs. To make a meaningful comparison, we interpolate our mass profiles at the radii corresponding to the locations of the other mass estimates.

eRosita

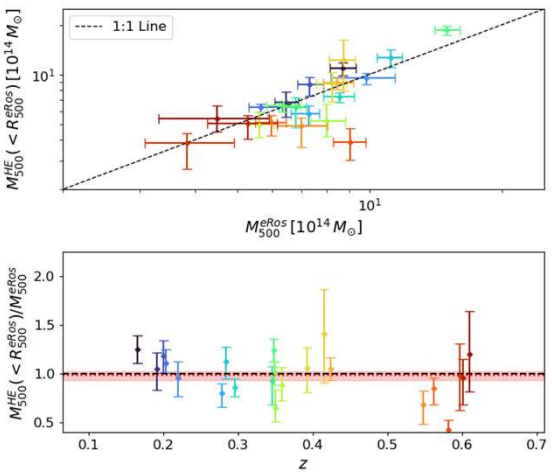

$$< \frac{M_{X,500}^{HE}}{M_{500}^{eRos}} > = 0.98 \pm 0.04$$

SPT

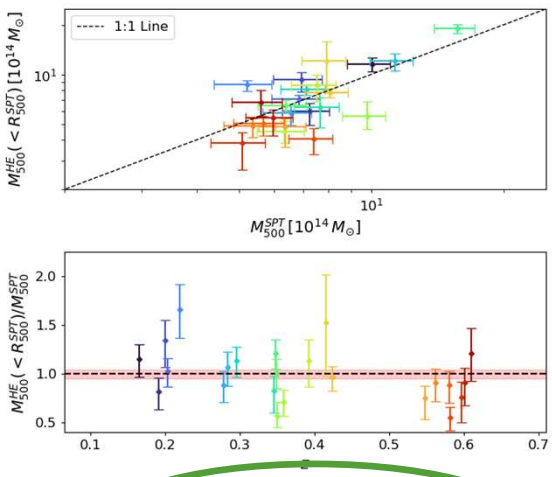

$$< \frac{M_{X,500}^{HE}}{M_{500}^{SPT}} > = 0.99 \pm 0.04$$

Planck

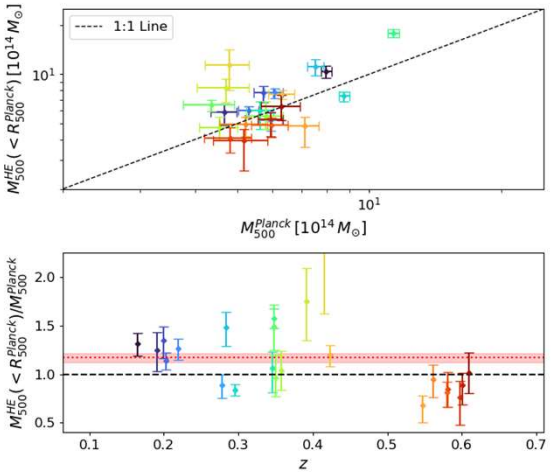

$$< \frac{M_{X,500}^{HE}}{M_{500}^{Planck}} > = 1.15 \pm 0.04$$

Hydrostatic mass bias or X-ray Cross-calibration issues?

On average, Chandra's temperatures are about 10-15% higher than those of XMM-Newton.
If the true temperature of a system is lower than Chandra's measurements, the true value would be lower, and consequently, these mass estimates would also be lower.

Hydrostatic gas fraction

- At each radius, we integrate the gas density profiles to determine the enclosed gas mass as:
  - $M_{gas}(< R) = \int_0^R 4\pi r^2 \rho_{gas}(r) dr$
- The hydrostatic gas fraction profiles are then computed as:
  - $f_{gas,\,i}^{HE}(R) = M_{gas}(< R)/M_i^{HE}\,(< R)$
- We compare our results with the universal gas fraction, that within a given radius can be written as

$$f_{gas,univ}(r) = Y_b(r)\frac{\Omega_b}{\Omega_m} - f_\star$$

with the universal baryon fraction from Planck Collaboration XIII (2016):

$$\Omega_b/\Omega_m = 0.156 \pm 0.003$$

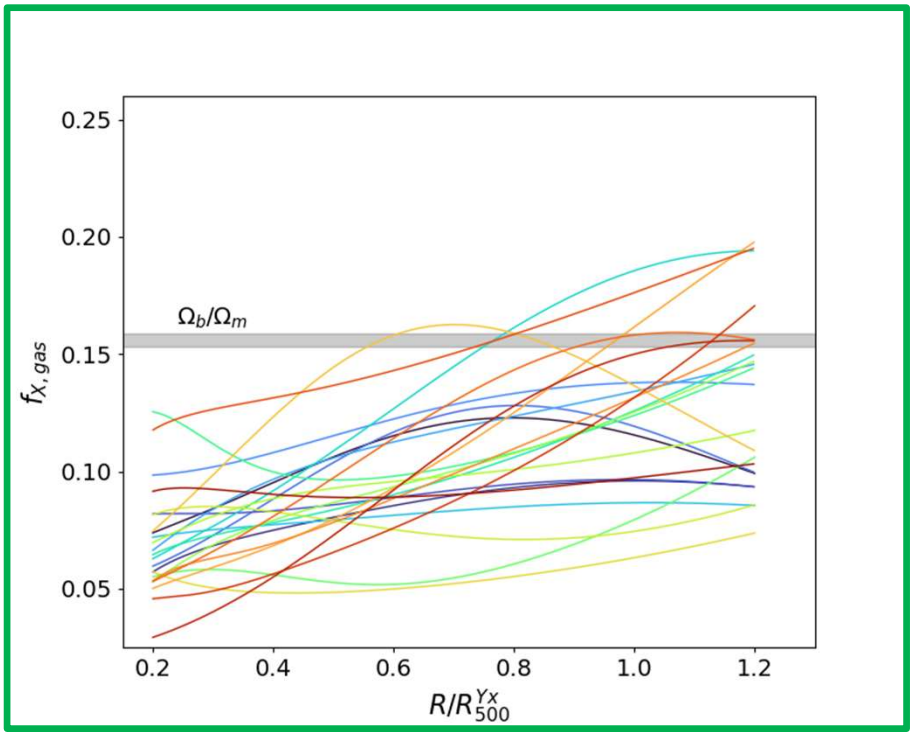

Hydrostatic gas fraction at R_{500}

We use our hydrostatic mass profiles to compute the hydrostatic gas fraction profiles and their value at the scale radius R_{500}^{HE}.
We then compare our results with the simulated universal gas fraction values from Eckert et al. (2019):

$$f_{univ,500} = Y_{b,500}\frac{\Omega_b}{\Omega_m} - f_{\star,500} = 0.131 \pm 0.009$$

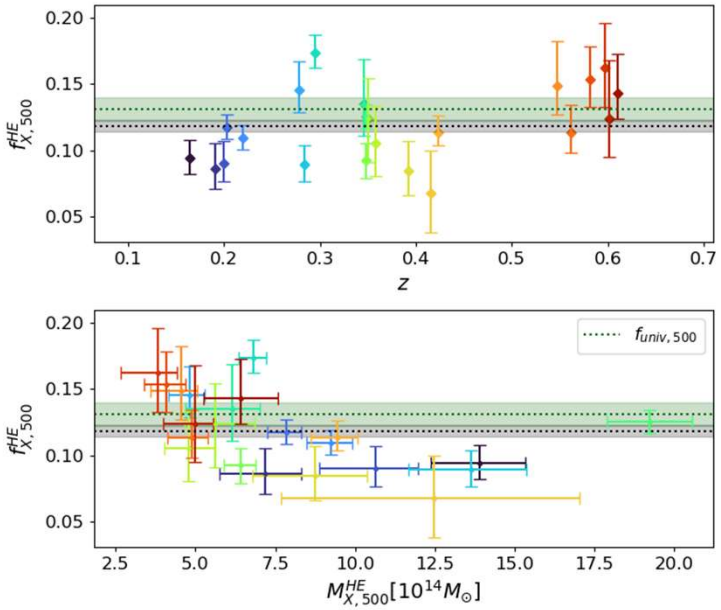

$$< f_{X,500}^{HE} > = 0.118 \pm 0.005$$

- **Lower value**

Possible systematics

Our gas fractions are approximately 15% lower then simulations. Similar to our mass estimates, these measurements are likely influenced by various systematics that can impact these comparisons.

Cross-calibration:

Chandra's temperatures are about 15% lower than XMM-Newton and eRosita. Chandra's temperature calibration tends to increase mass estimates systematically, which in turn lowers the derived hydrostatic gas fraction.

Molecular hydrogen column density:

If the total column density (atomic + molecular) is higher than the atomic hydrogen value we used, this would lead to an overestimation of the cluster temperature, impacting our Chandra-like estimates.

Relativistic Correction in SZ Analysis:

Neglecting relativistic effects could lead to an overestimation of the SZ signal, which in turn would result in higher pressure (i.e. higher inferred temperatures).

Selection Effects and Sample Size:

The limited sample size reduces the robustness of our statistical analysis, increasing the sensitivity to outliers or sample-specific features.

- **How can we get ICM properties (Thermodynamic profiles/Hydrostatic mass) in regions where X-ray spetroscopy fails?**

  - **Joint X-ray/mm approaches on cluster of galaxies:**

    Thermodynamic profiles, hydrostatic mass, gas fraction of high-z cluster and/or shallow X-ray observations.

- **Can a joint (X-ray/mm) analysis give new inputs on the cross-calibration issues?**

  - **Work in progress:**

    The lower gas fraction observed in our Chandra-like data, compared to simulations, represents an indication that Chandra temperatures may be overestimated.

    - Larger sample needed;
    - Different systematics to control.

Advantages of the pipeline

1) Constrain the thermodynamic profiles and hydrostatic mass across a wider radial range compared to an SZ-only or X-ray-only analysis. → **No need of spetroscopic temperature in the outskirts.**

2) Parametric modeling and local denoising of contaminants (CXB, GTD, CMB) → **Individual pressure (density) profile of high-redshift cluster.**

3) Extraction of the denoised SZ Maps in each frequency of Planck and SPT. → **Possibility to investigate eventual spectral distortion.**

4) Introduction of the normalization parameter η_T → **Take into account the possible systematic arising when different data-sets are combined.**

Results and discussion

- Our mass estimates **are consistent with the WL calibrated masses.** → **Individual mass and gas fraction profiles.**
- Our hydrostatic gas fraction are **lower than the prediction from simulations.**
- Our η_T value **is 20% higher** than previous estimates based on XMM-Newton. → **Information about the X-ray temperature cross-calibration issues.**

Work in progress

- Extending the analysis to **larger samples** (e.g. SPT-SZ catalog + Chandra observations).
  z > 1: SPT-Chandra joint fit. → We extract the thermodynamic profiles of a cluster at z=1.43
- Quantify the impact of the **column density** on the temperature / η_T of our sample.
- Implementation of the **Relativistic corrections**.

Future perspective

- Combination and comparison with other X-ray and millimetric instruments (eRosita, XMM-Newton, Nika2).
- Scientific inferences from the individual thermodynamic profiles (e.g. evolution, dynamical indicator)
- Non-thermal pressure support / hydrostatic mass bias on our mass / gas fraction estimates

Advantages of the pipeline

1) Constrain the thermodynamic profiles and hydrostatic mass across a wider radial range compared to an SZ-only or X-ray-only analysis. → **No need of spetroscopic temperature in the outskirts.**

2) Parametric modeling and local denoising of contaminants (CXB, GTD, CMB) → **Individual pressure (density) profile of high-redshift cluster.**

3) Extraction of the denoised SZ Maps in each frequency of Planck and SPT. → **Possibility to investigate eventual spectral distortion.**

4) Introduction of the normalization parameter η_T → **Take into account the possible systematic arising when different data-sets are combined.**

Results and discussion

- Our mass estimates **are consistent with the WL calibrated masses.** → **Individual mass and gas fraction profiles.**
- Our hydrostatic gas fraction are **lower than the prediction from simulations.**
- Our η_T value **is 20% higher** than previous estimates based on XMM-Newton. → **Information about the X-ray temperature cross-calibration issues.**

Papers and Conferences

C. Mastromarino, F. De Luca, H. Bourdin, P. Mazzota, “Hydrostatic Mass and Baryon Fraction of Galaxy Clusters: A Joint X-ray and Millimeter Analysis of 23 SPT-SZ Selected Clusters", (Under int. review)

C. Mastromarino, F. Oppizzi, F. De Luca, H. Bourdin, P. Mazzota, (2024), “Resolving high-z Galaxy Cluster properties through joint X-ray and Millimeter analysis: a case study of SPT-CLJ0615-5746.“A&A, 688, A76. https://doi.org/10.1051/0004-6361/202449422

C. Mastromarino, G. Despali, L. Moscardini, A. Robertson, M. Meneghetti, M. Maturi (2023) “Properties and observables of massive galaxies in self-interacting dark matter cosmologies.", Monthly Notices of the Royal Astronomical Society, 524(1),1515-1528, DOI: 10.1093/mnras/stad1853

G. Despali, F. Heinze, **C. Mastromarino** (2022)“Gravitational lenses in hydrodynamical simulations", Proceedings of the International Astronomical Union, 18(S381), 41-45

1st,2nd, 3rd year AASS PhD Workshop, (2022, 2023, 2024), Roma

“CLUSTER4 national conference” 2024, Trieste;

GALAXY GROUPS IN THE ERA OF EROSITA AND EUCLID: A MULTIWAVELENGTH VIEW, 2024, Sexten;

eROSITA-day / groups clusters, 2024, Bologna

“Astronomy, Astrophysics and Space Science Journal Club”, 2023, Roma.

“CLUSTER3 national conference” 2022, Bologna;

“1st Mondragone Frontiers of Astronomy Series: latest advances in X-ray spectroscopy and polarimetry” 2022, Roma;

Backup Slides

Thermodynamic profiles of galaxy clusters

Galaxy cluster represent the most massive gravitationally bound structures: $10^{14}\ M_{\odot} \leq M_{Tot} \leq 10^{15}\ M_{\odot}$.

- **Galaxies** : ~ 3 % of the total mass
- **Intra-cluster medium** : ~ 17 % of the total mass
- **Dark Matter**: ~ 80 % of the total mass

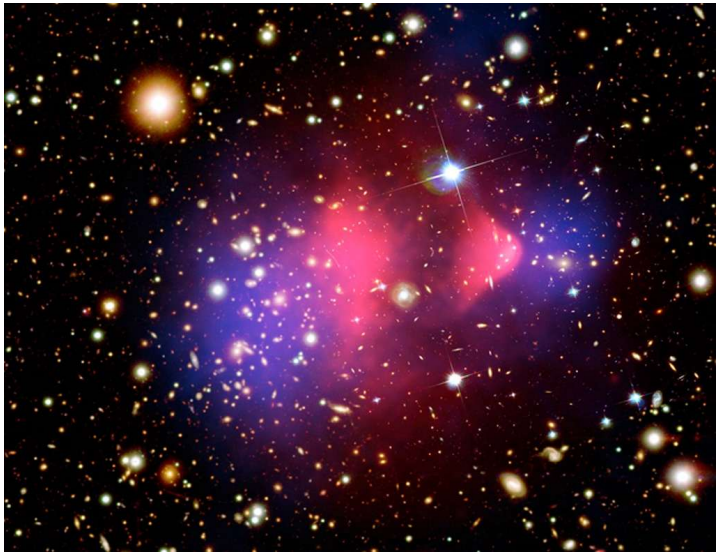

X-ray: NASA/CXC/CfA/M.Markevitch,
Optical and lensing map: NASA/STScI,
Magellan/U.Arizona/D.Clowe.

Resolve the **ICM** properties allows us to understand the physical mechanism of the interplay between baryons and DM and their dependence on redshift.

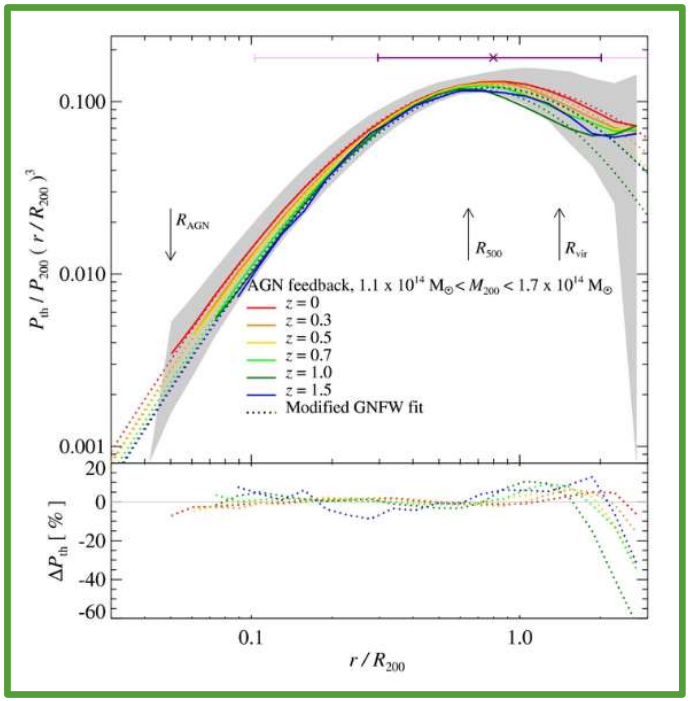

Redshift evolution of simulated pressure profiles.
Credit: Battaglia et al. (2012)

X-ray density fitting

1. We use the X-ray peak to compute all the radial profiles of the background-subtracted X-ray observable: the surface brightness (Σ_X) and the spectroscopic temperature (T_X).
2. We then parameterize the emission measure $[n_p n_e](r)$ and the temperature $T(r)$ profiles using analytical forms first proposed in Vikhlinin et al. (2006) and integrated them along the line of sight and fitted to the two observable profiles (Σ_X and T_X).
3. All the fits are conducted with a least-squares minimization. For uncertainties envelopes, we perform 500 parametric bootstrap realizations of the observed profiles, estimated considering 8 radial bins inside R_{200} for T_X and 30 radial bin for Σ_X.

$$n_p n_e(r) = \frac{n_o^2 (r/r_c)^{-\alpha}}{[1+(r/r_s)^\gamma]^{\epsilon/\gamma}[1+(r/r_c)^2]^{3\beta_1-\alpha/2}} + \frac{n_{0,2}^2}{[1+(r/r_{c,2})^2]^{3\beta_2}}$$

$$T(r) = T_0 \frac{x + T_{min}/T_0}{x+1} \frac{(r/r_t)^{-a}}{[1+(r/r_t)^b]^{c/b}}$$

X-ray density fitting

$$\Sigma_X(r_{2D}) = \frac{1}{4\pi(1+z)^3} \int \frac{n_e^2(r_{3D})}{x} \Lambda(T, Z)\, dl$$

To test this dependency, we test how different temperature at high radii can impact the final density profiles.

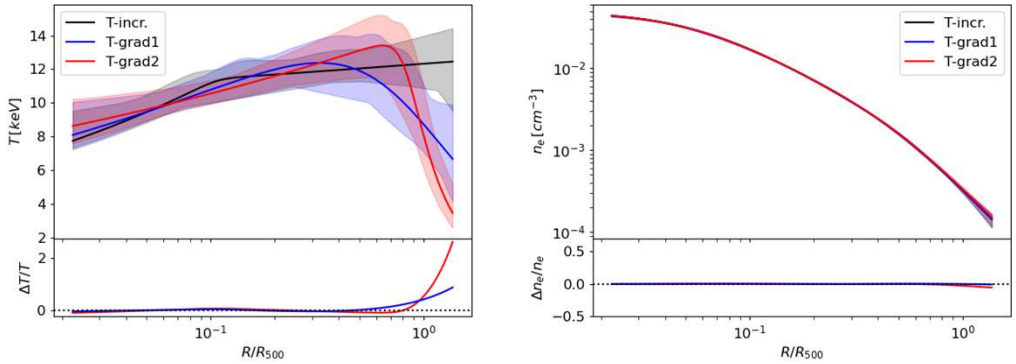

We can constrain the density profile up to R_{200} without knowing the exact temperature profile.

Planck processing

We use data from the second public data relase PR2, extracted using Planck HFI data from the full 30-months mission:

100 GHz	143 GHz	217 GHz	353 GHz	545 GHz	857 GHz

1. All-sky HFI frequency maps have been reprojected on smaller tiles of 512 × 512 pixels into the tangential plane, with the resolution of 1 $arcmin/pixel$ around the X-ray peak of the cluster.

2. These maps incorporate both the SZ signals, but also dust contaminations and CMB anisotropies. We isolate the SZ cluster signal, following Bourdin et al. 2017.

3. To create a spatial template for the Galactic thermal dust anisotropies (GTD), we denoise the 857 Ghz map.

4. To construct the spatial CMB template, we subtract the GTD template from the denoised 217 GHz map .

5. Both the GTD and CMB templates are then re-scaled to all HFI frequencies and jointly fitted to the data extracted in the where no cluster signal is expected.

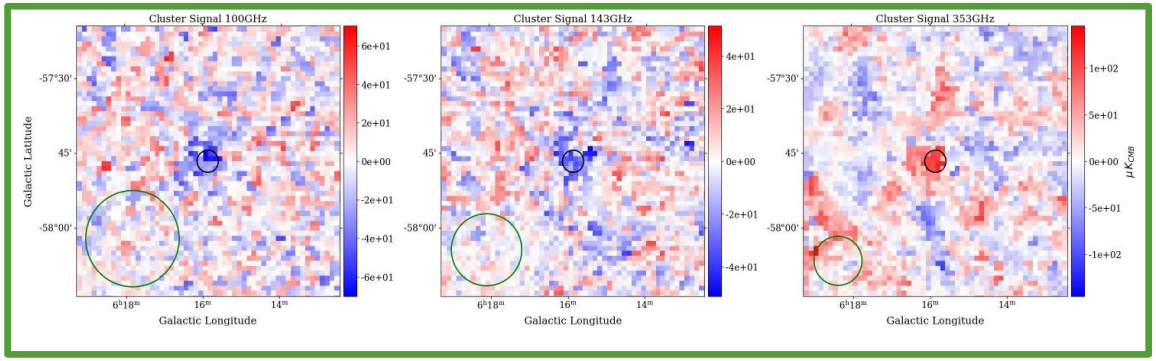

SPT processing

We use public SPT data from the 2500-square degree SPT-SZ survey:

95 GHz	150 GHz	220 GHz

1. We use the public SPT maps, reprojected on smaller tiles of 1024 × 1024 pixels into the tangential plane, with the resolution of 0.5 $arcmin/pixel$.

2. Here, we do not have the high frequency channels. We recover the CMB signal using the ILC method with a linear combination of the three SPT frequency maps and the 217 GHz map from Planck.

3. Assuming that the data can be represented as a linear combination of different component (linear mixture model), the key of the ILC is determining the optimal coefficients of the LC to minimize the contamination from foreground emissions and instrumental noise while preserving the CMB signal.

4. We calculate the coefficients of the LC on a sub-region around the X-ray peak. Then we convolve the map estimation of the CMB with the corresponding PSF to obtain the CMB template for each channel.

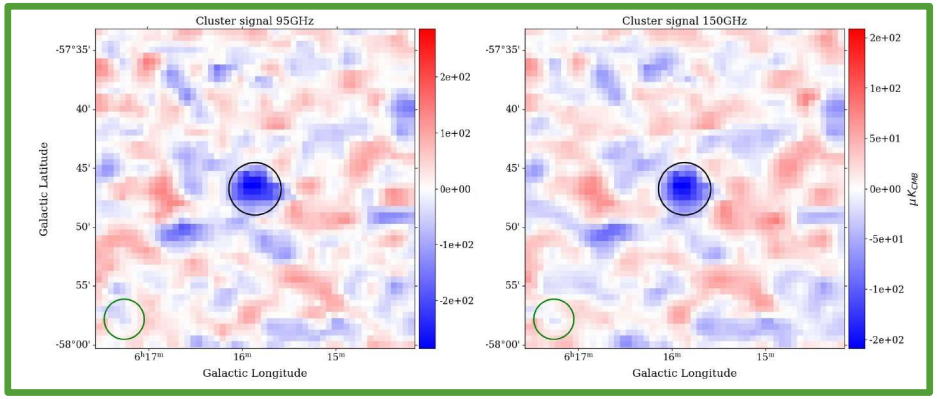

SZ-only vs Joint Fit

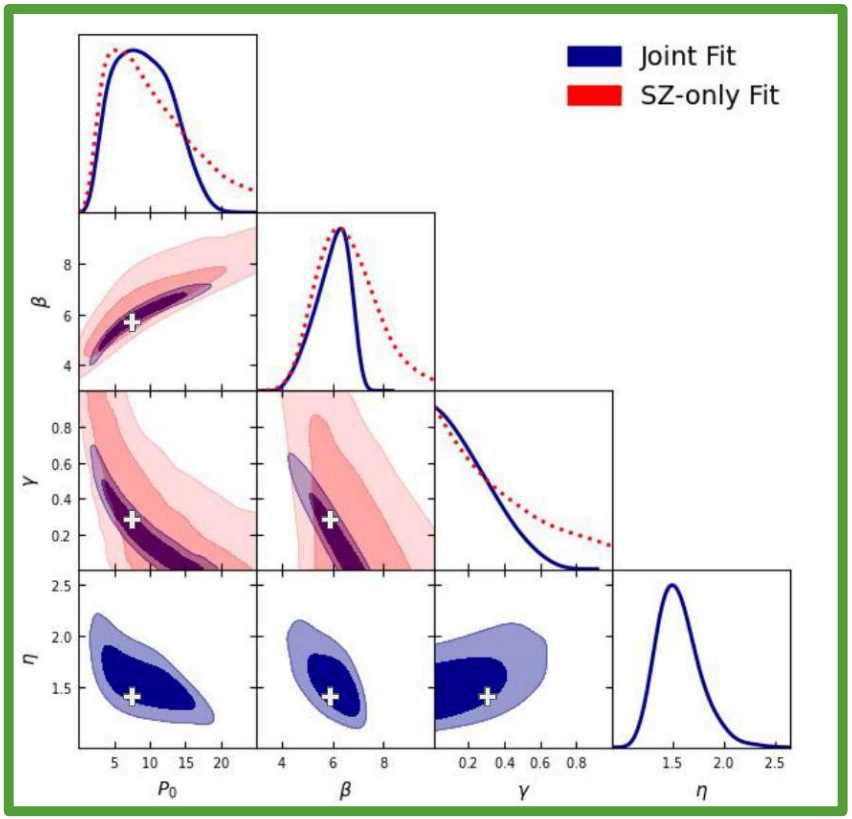

- Aside from extending the radial coverage at high radii respect to an X-ray only analysis, we show that the joint fit **improves also the constrains of the pressure profile in the central region of the cluster**, respect to an SZ-only analysis.
- Due to the limited resolution of SPT and Planck with an SZ-only fit we are not able to put proper constrain on all the parameter of the Nagai profile that we want to fit.
- We find that the only effective approach to achieve the convergence of the chain and obtain reliable constrain on the parameters is to **fix gamma**.
- Our joint fit improved this constrains especially in the central region. Where this improvement is manly attributed to the high resolution of Chandra, allowing **to better constrain the shape of the pressure profile within R_{500}**

Internal Linear Combination

The ILC (Internal Linear Combination) method is a technique used in Cosmic Microwave Background (CMB) analysis to derive a cleaned CMB signal from observed maps.
The ILC method averages the frequency information to construct a linear combination of the available data sets that optimally separates the CMB signal from the contaminating sources. This linear combination is usually represented as follows:

$$CMB_c = \sum_i w_i \, data_i$$

Here, CMB_c is the derived CMB signal, $data_i$represents the observed maps from frequencies, and w_i are the weights assigned to each data set.
The key to the ILC method is determining the optimal weights, w_i , for each data set to minimize the contamination from foreground emissions and instrumental noise while preserving the CMB signal.
These weights are computed in such a way that the resulting combination minimizes the variance of the cleaned map.

In our case The LC weights are computed to minimize the variance with respect to a signal constant in frequency (i.e. the CMB) and simultaneously to null the non-relativistic SZ component. Assuming that the data can be represented as the linear combination of different components (the so-called linear mixture model) the conditions lead to the solution:

$$\boldsymbol{w} = \frac{\boldsymbol{eC^{-1}}}{\boldsymbol{A^T C^{-1} A}}$$

in this notation, the elements of the vector w correspond to the weights assigned to each frequency, C is the data covariance matrix between the N_{chan} channels, e is a vector of ones of length
N_{chan} and A is a N_{chan} × 2 matrix accounting for the emission
the CMB and the SZ signal at the various frequency.

$$A = \begin{pmatrix} 1 & s_{SZ,0} \\ \vdots & \vdots \\ 1 & s_{SZ,N_{chan}} \end{pmatrix}$$

Fitting procedure

We calculate the best fit and confidence intervals we employed the Cobaya MCMC framework with a Gaussian log-likelihood as the sum of the two independent data-sets ($\ln \mathcal{L} = \ln \mathcal{L}_{SZ} + \ln \mathcal{L}_X$):

$$\ln \mathcal{L}_{SZ}(\theta) \propto \sum_i \left(y_i - I_{SZ,i}\right)^T C_i^{-1} \left(y_i - I_{SZ,i}\right)$$

$$\ln \mathcal{L}_X(\theta) \propto \sum_i \left(T_{X,i} - \widetilde{T}_i\right)^2 \times \frac{1}{\sigma_{X,i}^2}$$

where y_i represent the measured SZ profiles along with the associated template $I_{SZ,i}$ and the covariance matrix C_i accounts for both instrumental noise and correlations between channels.
In the X-ray likelihood, $T_{X,i}$ represent the spetroscopic temperatures with respective errors $\sigma_{X,i}$, while $\widetilde{T}_i$ represent the temperature template projected along the line of sight.
Here, $\theta = [P_0, c_{500}, \alpha, \beta, \gamma, \eta_T]$ is the vector with the parameters of our model.

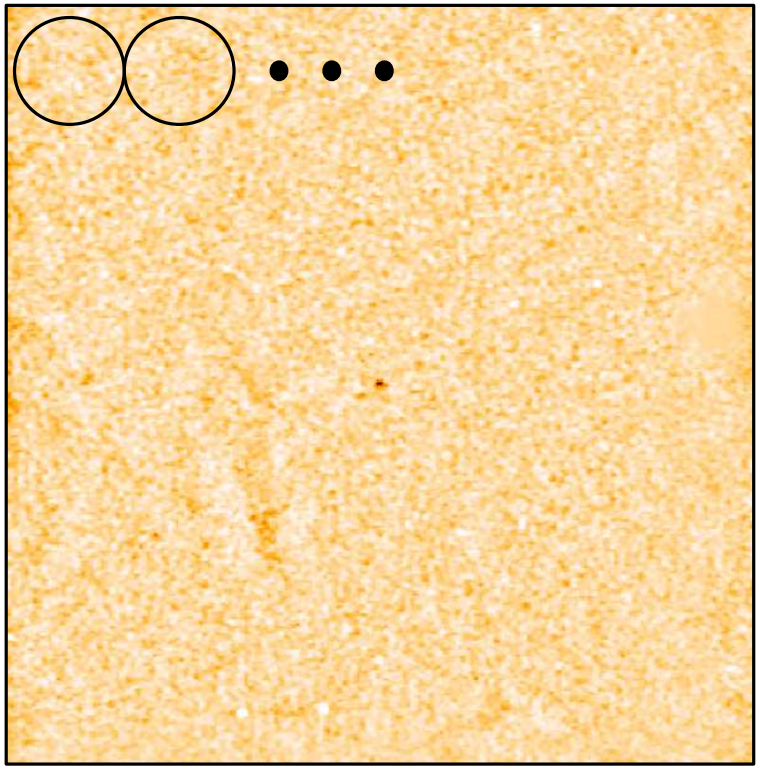

Since we recover the CMB using a LC of channels, the noise from one map could leak into the other through the background subtraction step. We calculate 100 profiles on the cleaned maps, in regions treated with the same cleaning technique but where we do not expect to find the cluster signal. For both instruments, we concatenate the profiles calculated on each map and we compute the covariance between all these profiles.

SZ-like hydrostatic mass

We compare the hydrostatic mass estimates obtained from our joint fit with other mass estimates derived from other catalogs. To make a meaningful comparison, we interpolate our mass profiles at the radii corresponding to the locations of the other mass estimates.

eRosita

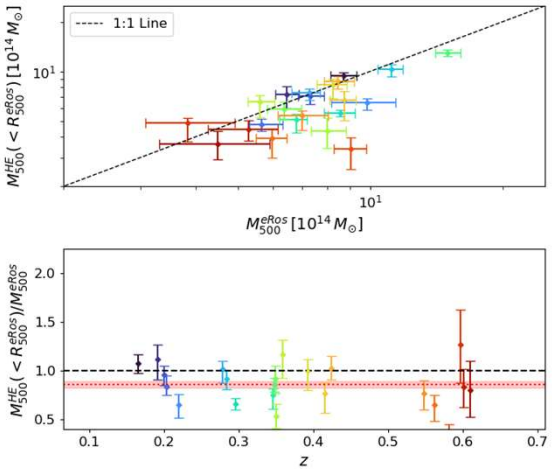

$$< \frac{M_{SZ,500}^{HE}}{M_{500}^{eRos}} > = 0.86 \pm 0.03$$

SPT

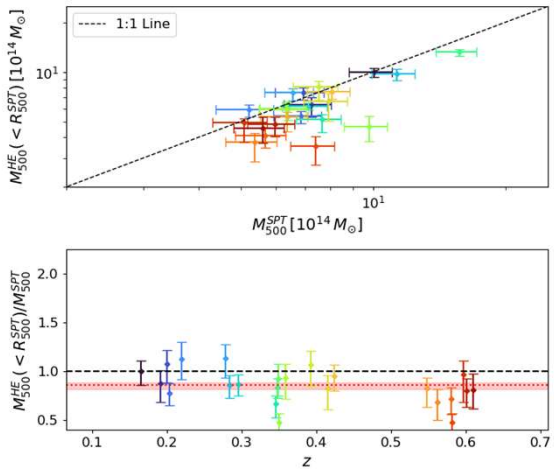

$$< \frac{M_{SZ,500}^{HE}}{M_{500}^{SPT}} > = 0.86 \pm 0.03$$

Planck

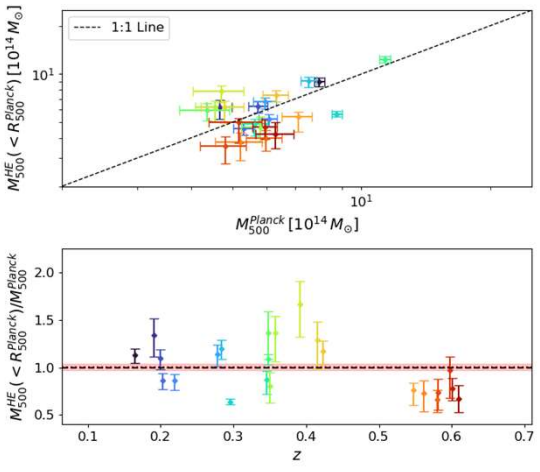

$$< \frac{M_{SZ,500}^{HE}}{M_{500}^{Planck}} > = 1.01 \pm 0.03$$

- Our SZ-like hydrostatic mass are around 14% lower than the mass estimates from SPT and eRosita catalogs (**WL calibrated masses**). Aligns with the known **hydrostatic mass bias**, where hydrostatic mass measurements are typically lower than weak lensing masses due to the assumption of hydrostatic equilibrium, which may not fully hold in actual cluster conditions.

- Our SZ-like masses are consistent with the mass esitmates from Planck catalog.

Comparison with other catalogs

We compare the hydrostatic gas fraction estimates obtained from our joint fit with other gas fraction estimates derived from other catalogs. For each catalog we only consider the M_{500}^{i} and respective R_{500}^{i} and we calculate the f_{500}^{i} as:

$$f_{500}^{i} = \frac{M_{gas}(< R_{500}^{i})}{M_{500}^{i}}$$

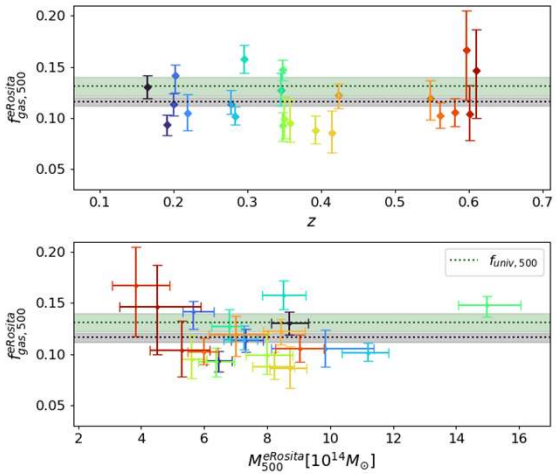

$< f_{500}^{eRosita} > = 0.116 \pm 0.004$

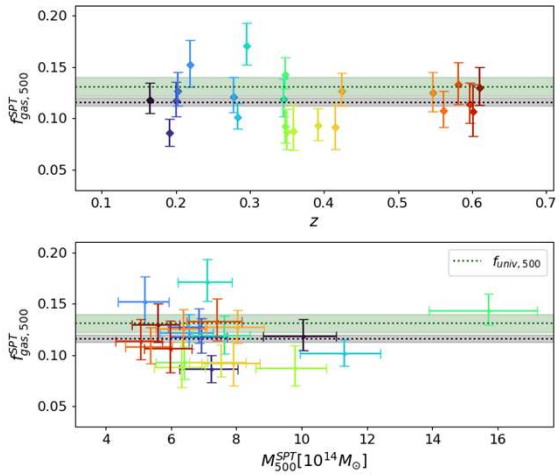

$< f_{500}^{SPT} > = 0.116 \pm 0.004$

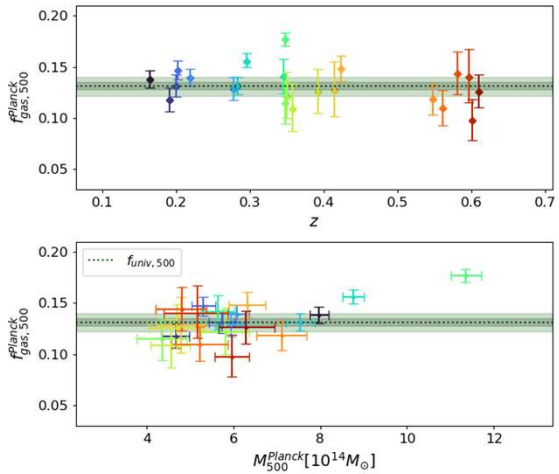

$< f_{500}^{Planck} > = 0.131 \pm 0.004$

- Both the gas fraction from eRosita and SPT catalog are lower than the universal value from Eckert et al. (2019). They are in agreement with our Chandra-like estimates.
- The gas fraction from Planck catalog are in agreement with both the universal value and our SZ-like estimates.

M_{500}^{eRos} from the catalog (maximum posterior)

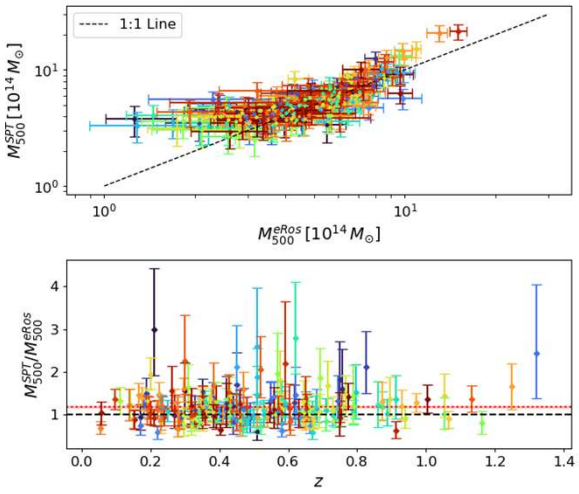

$$< \frac{M_{500}^{SPT}}{M_{500}^{eRos}} > = 1.18 \pm 0.03$$

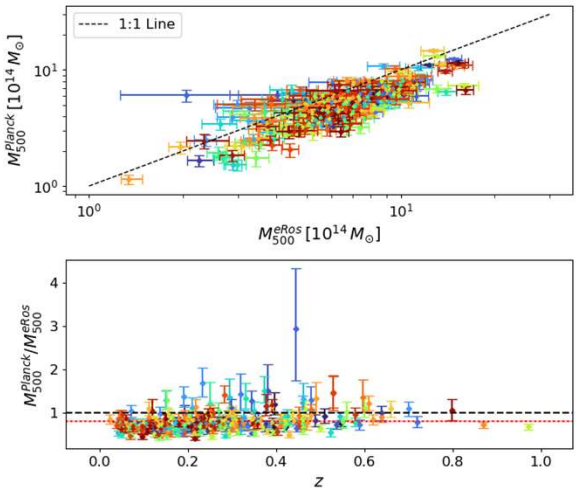

$$< \frac{M_{500}^{Planck}}{M_{500}^{eRos}} > = 0.81 \pm 0.01$$

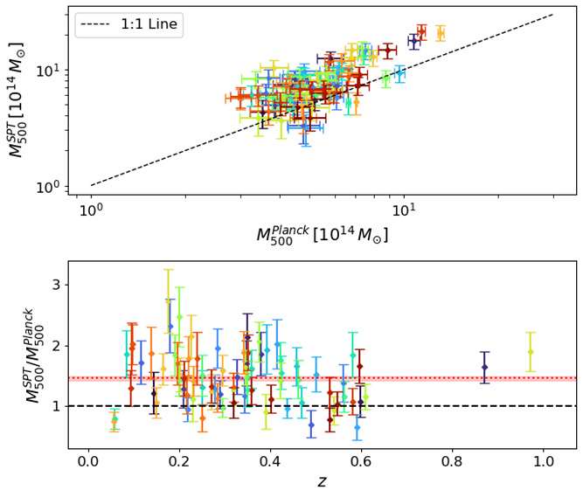

$$< \frac{M_{500}^{SPT}}{M_{500}^{Planck}} > = 1.45 \pm 0.03$$

M_{500}^{eRos} from PDF

$$M_{500}^{eRos} = \int M\,P(M)dM \Big/ \int P(M)dM$$

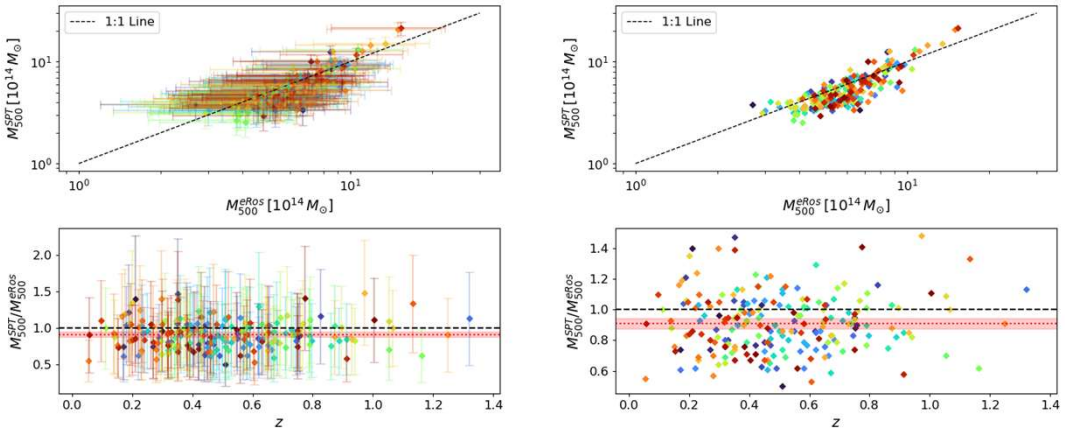

$$< \frac{M_{500}^{SPT}}{M_{500}^{eRos}} > = 0.91 \pm 0.03$$

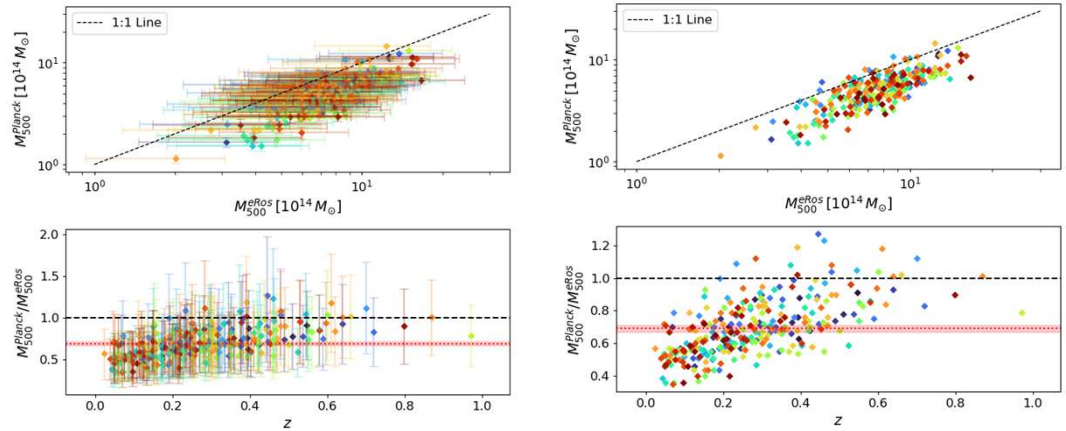

$$< \frac{M_{500}^{Planck}}{M_{500}^{eRos}} > = 0.69 \pm 0.02$$